Damped superconducting structure for EUV light source based on energy recovery linac

Taro Konomi,* Kensei Umemori, Hiroshi Sakai, and Eiji Kako
High Energy Accelerator Research Organization, KEK, 1-1 Oho, Tsukuba, Ibaraki 305-0801, Japan

Tomoko Ota and Atsushi Miyamoto
Toshiba Energy Systems and Solutions Corporation, 72-34 Horikawa-cho, Saiwai-ku, Kawasaki 212-8585, Japan

(Received 18 January 2023; revised 26 September 2023; accepted 21 November 2023; published 15 December 2023)

A 10-kW-class high-power extreme ultraviolet light source is required in mass microfabrication technologies, and a free-electron laser based on an energy recovery linac (ERL) is an attractive candidate. The design beam current is 9.75 mA, and the beam energy is 800 MeV. The cavity design is required to achieve a target gradient of 12.5 MV/m with a high yield and efficient suppression of radiofrequency power losses through higher-order modes (HOMs). The HOMs generated in the cavity pass through the end cells and are damped by the beam-tube dampers. The cavity was designed mainly to reduce the heat generated by the monopole modes. Further, the transverse shunt impedance of dipole modes must be smaller than the specification related to the beam breakup effect. Considering the cavity design, the end cell was optimized by selecting the appropriate frequency obtained using the tuning curve method. The shape of the HOM damper was designed using the complex permittivity data obtained from the S-parameter method with sample pieces. This cavity design was confirmed to have a sufficient margin of accelerating gradient and adequately damped HOMs for the 10-mA-class ERL operation.

DOI: 10.1103/PhysRevAccelBeams.26.121601

I. INTRODUCTION

The application of mass microfabrication technology to the production of integrated circuits using techniques such as photolithography has been the subject of constant improvement. Next-generation photolithography technology using extreme ultraviolet (EUV) light with a wavelength of 13.5 nm has been developed to achieve narrow line widths (less than 10 nm). However, numerous unresolved problems must be addressed before mass production can be realized. For this purpose, a 10-kW-class high-power laser is required as the EUV light source, and a free-electron laser (FEL) based on an energy recovery linac (ERL) is the most suitable candidate [1–5]. An ERL recovers energy by decelerating the accelerated beam after use [6,7]. Energy is recovered by using superconducting radiofrequency (SRF) cavities, which are associated with low rf losses across the cavity walls. This principle has been proposed and demonstrated in many systems [8,9], including a compact-ERL (cERL) at the High Energy Accelerator Research Organization (KEK) in Japan [10].

Various types of multicell SRF cavities have been designed for ERLs, such as cERL [11], bERLinPro [12], CBETA [13], and eRHIC (EIC) [14] for a 100-mA-class ERL, which have focused on increasing the maximum threshold beam current. The extraction of higher-order-mode (HOM) power is a key issue in maintaining beam quality, and HOM damping structures such as the HOM coupler, waveguide coupler, and beam-tube damper have been considered. In particular, the cERL has two SRF nine-cell cavities, and its HOM parameters are optimized for a 100-mA-class ERL. Each cavity contains nine elliptical cells flanked by eccentric fluted beam tubes with two adjoining HOM dampers [15]. An iris diameter of 80 mm enables the strong damping of the HOMs. Although the cERL cavity possesses sufficient margins for HOM beam breakup (BBU), the accelerating gradient has been limited to between 8 and 10 MV/m during beam operation because of heavy field emission [11]. The ratio of the surface peak electric field (E_{sp}) and the accelerating gradient (E_{acc}) was 3.0 such that the maximum surface peak field was attained between 24 and 30 MV/m.

Various ERL cavities have been designed for a 100-mA-class beam current to replace synchrotron radiation light source rings. However, the EUV-FEL requires a 10-mA-class

*konomi@frib.msu.edu
Present address: Facility for Rare Isotope Beams, Michigan State University, East Lansing, MI, USA.

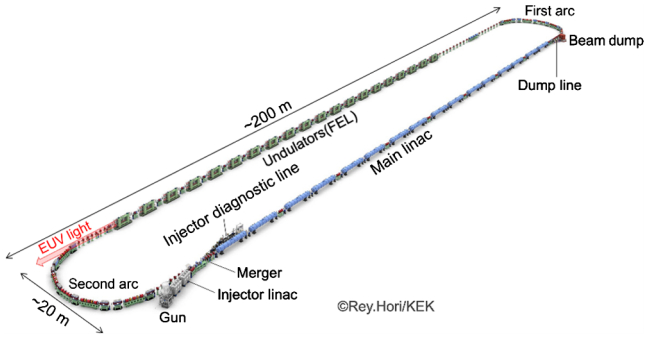

FIG. 1. Conceptual design of an EUV-FEL accelerator (output power of 10 kW, as shown in [5]). This EUV-FEL accelerator follows a racetrack-type layout. The injected beam is accelerated in the main linac and is compressed in the arc and chicane sections. An EUV light is emitted at the undulator line. Subsequently, the beam energy is recovered by the main linac and dumped at the beam dump.

beam current. Therefore, designing cavities suitable for the 10-mA class is effective; further, relaxing the HOM requirements and lowering the E_{sp}/E_{acc} ratio enables stable operation.

The design of the EUV-FEL light source accelerator is based on the observed features of the cERL during operation. Figure 1 and Table I show the conceptual design of the EUV-FEL accelerator and accelerator parameters, respectively [5]. The EUV accelerator follows a racetrack-type layout, and the injector energy is 10 MeV. The injection beam is accelerated by the SRF cavities in the main linac and compressed at the arc and chicane. The undulator line emits EUV light. Subsequently, the beam energy is recovered by the main linac. The SRF cavities and undulators are located in the two long, straight sections. A beam energy of 800 MeV is suitable for generating a 13.5 nm EUV-FEL, and the total beam current passing through the SRF cavity is 19.5 mA. The desired accelerating gradient of the nine-cell SRF cavities is 12.5 MV/m. The effective length of one nine-cell cavity is approximately 1 m. A total of 64 units of SRF cavities are required to accelerate the beam up to 800 MeV. A high bunch charge of 60 pC and a high repetition rate of 162.5 MHz are required to achieve a 10-kW-class high-power EUV-FEL. A bunch length of 1 to 2 ps is considered at the SRF cavity section. This bunch is compressed to several tens of femtoseconds at the first arc and chicane sections and decompressed at the second arc section for efficient energy recovery without significant beam loss. The SRF cavities for the EUV light need to possess sufficient margins for stable operation. The target value of E_{sp}/E_{acc} for the EUV cavity is set at 2.0.

TABLE I. Beam and SRF cavity parameters of the EUV-FEL accelerator. The repetition and current parameters shown correspond to the undulator. Because the beam passes through the SRF cavity twice for acceleration and deceleration, the repetition and current values are doubled.

Parameter	Values
Wavelength	13.5 nm
Output power	10 kW
Bunch charge	60 pC
Beam energy	800 MeV
Beam repetition	162.5 MHz
Beam current	9.75 mA
Accelerating gradient	12.5 MV/m
Design Q value	1×10^{10}
Number of SRF cavities	64 × 9-cell cavity
Total cavity heat load at 2 K	991 W

In this study, based on our experience with cERL cavities, we designed a new SRF cavity with high stability and low risk for field emission suitable for 10-mA-class EUV-FEL accelerators. A simple axisymmetric cavity and HOM damper shape are required to achieve a high gradient without field emission along with efficient HOM damping to realize reliable operation for industrial applications. We evaluated the high impedance and harmful low-frequency HOMs such as TE111, TM110, and TM011 to determine the best cavity and HOM damper shape.

The remainder of this paper is organized as follows: First, the design concept of the cavity structure is summarized in Sec. II. The selection of the center-cell shape and beam-tube diameter and the method of end-cell shape optimization for the HOM modes are described in Sec. III. The HOMs of TE111, TM011, and TM110 and the optimized cavity shape are presented in Sec. IV. In Sec. V, we discuss the HOM damper design based on material measurement data and present the evaluation of the final HOM with the designed EUV nine-cell cavity. This is followed by a brief discussion of the EUV cavity structure. Finally, in Sec. VI, we present the conclusions.

II. DESIGN CONCEPT OF EUV CAVITY

The beam induces wakefields in the superconducting accelerating cavity. These wakefields are stored in the cavity as HOMs, which have to be sufficiently damped to avoid beam instability. The configuration of the EUV cavity considered in this study is shown in Fig. 2. The shape of the center cell is the same as that of the TESLA

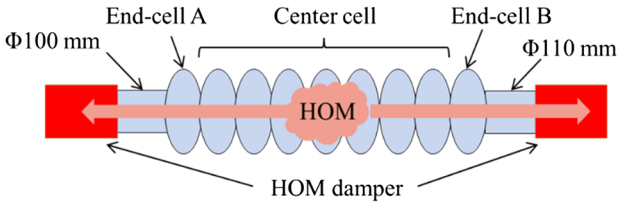

FIG. 2. Conceptual design of the EUV nine-cell cavity. The HOMs are propagated through both end cells and damped by the HOM dampers at the beam tubes. The rf field distribution is actively shifted by making the beam-tube diameter asymmetrical and biasing the HOM field distribution.

cavity [16]. The E_{sp}/E_{acc} ratio of the TESLA cavity is 2.0 and has been validated for high-gradient operations in many studies. The ratios R/Q and E_{sp}/E_{acc} of the accelerating mode are strongly dependent on the shape of the center cell. The accelerating mode parameters of the investigated EUV cavity are almost the same as those of the TESLA cavity.

The HOM frequencies must not be integral multiples of the beam repetition frequency to suppress the stacking of the HOMs. Additionally, the target heat load of the HOMs must equal several tens of watts to realize an HOM. The maximum power ($P_{b,max}$) achieved by stacking the HOMs is expressed as

$$P_{b,max} = R/Q \times Q_{ext} \times I_0^2, \tag{1}$$

where I_0 is the beam current passing through the cavity. The beam current in the EUV cavity used in this study was 19.5 mA. The product $R/Q \times Q_{ext}$ represents the shunt impedance of the monopole HOMs. The EUV cavity was designed by prioritizing the minimization of Q_{ext} because R/Q is dependent on the center cell, and its change is negligible.

The longitudinal shunt impedance R/Q of the monopole HOM is defined by the following equation in [17]:

$$\frac{R}{Q} = \frac{V^2}{\omega_n U} = \frac{|\int_0^d E_z(\rho=0)e^{i\omega_n z/v}dz|^2}{\omega_n U}, \tag{2}$$

where V is the longitudinal voltage of the HOM field, ω is the angular frequency, U is the stored energy, d is the cavity length, v is the longitudinal velocity of charge, n is the HOM number, and E_z is the longitudinal electric field on the beam axis ($\rho = 0$).

The transverse shunt impedance R_t/Q of the dipole HOM is defined by the following equation in [17]:

$$\frac{R_t}{Q} = \frac{V_\perp^2}{\omega_n U} = \frac{|\int_0^d E_z(\rho=a)e^{i\omega_n z/v}dz|^2}{(k_n a)^2 \omega_n U}, \tag{3}$$

where $V_\perp$ is the transverse voltage, $k_n = \omega_n/c$, and E_z is the longitudinal electric field at a distance of $\rho = a$ from the beam axis. In this study, the transverse field was calculated at $a = 1$ mm.

The damped power of the HOM damper is assumed to be up to 100 W, and a 100-W-class HOM damper has been developed for cERL [18,19]. A modified HOM damper is developed and used for the EUV cavity in this study. The longitudinal shunt impedance of the longitudinal HOMs must be less than $1.31 \times 10^5\ \Omega$ [based on Eq. (1)] in the worst-case scenario wherein the HOM frequency matches the beam repetition rate.

The target impedance of the dipole HOMs was determined from the BBU threshold [20]. The threshold beam current of the EUV accelerator was evaluated using the existing cavity model, which was designed as a prototype for the KEK-ERL project and is called the KEK Model-1 cavity [18,19]. The KEK Model-1 cavity has TESLA cells, and one side of the beam-tube diameter was increased from 78 to 108 mm. The highest transverse shunt impedance of the KEK model-1 cavity was $5.5 \times 10^4\ \Omega\,\mathrm{cm}^{-2}\,\mathrm{GHz}^{-1}$. The HOM-BBU threshold current was calculated for the five strongest transverse HOMs of the KEK model-1 cavity and the designed main-linac optics of the EUV-FEL light source, as shown in [3]. By scanning over the betatron phase advance ($0 - 2\pi$) and return loop length (in one rf period), the minimum threshold current was estimated to be 195 mA by using a simulation code bi [21] even without HOM frequency randomization (the BBU threshold current can increase up to 1.1 A with a frequency spread of 2 MHz in rms). This is 1 order of magnitude higher than the EUV operation current. Therefore, the target value of the transverse shunt impedance for the EUV cavity design is considered equivalent to that of the KEK model-1 cavity (i.e., $5.5 \times 10^4\ \Omega\,\mathrm{cm}^{-2}\,\mathrm{GHz}^{-1}$).

The structure of the EUV cavity is shown in Fig. 2. The cavity consists of nine cells of 1.3 GHz, similar to the cERL [18,19] developed at KEK. Using a 1.3 GHz nine-cell system, the existing facilities such as surface treatment equipment can be used. The HOMs induced in the cavity cell propagate through both end cells and are damped at the beam-tube damper. All HOMs are assumed to be damped effectively if the frequencies of the end cells match those of the center cells. If the frequencies of the center and end cells do not match, the rf power is trapped in the center cells. We determined that matching all HOM frequencies for the end and center cells is difficult because of parameter constraints associated with the cavity shapes. Consequently, the design of the proposed system was focused on low-frequency HOMs, which had frequencies that could be controlled relatively easily during fabrication. The diameters of the beam tubes were asymmetrically set to actively shift the rf field distribution and increase the damping efficiency.

III. DESIGN OF EUV CAVITY

A. Center-cell shape

The TESLA-type center-cell shape was slightly modified for fabrication, as shown in Fig. 3(a). Straight sections of 1 mm were added at the iris and equator. Both the elliptical shape and length of the iris and equator were adapted to approximate the shape and length of a TESLA cavity. Figure 4 displays the dispersion curve of the center cell obtained using the CST-MW studio [22]. The frequencies corresponding to 0° and 180° were calculated using the electric and magnetic boundary conditions, respectively, at the iris. The relationship between the frequencies corresponding to 0° and 180° is expressed by the following equation:

$$f = f_0\left\{1 + \frac{k_c}{2}(1 - \cos\theta)\right\}, \tag{4}$$

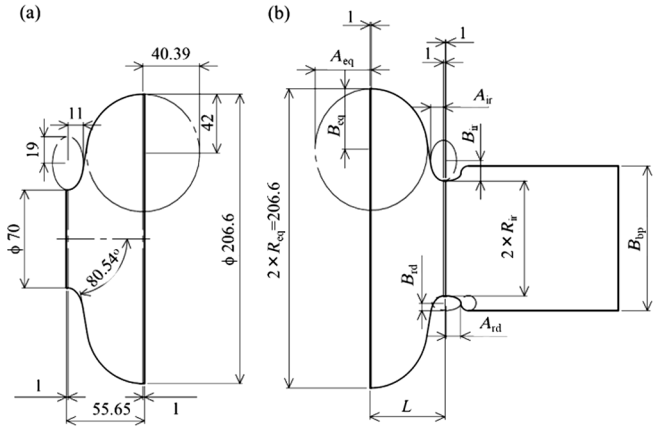

FIG. 3. Design of the cavity cell shapes for the EUV light source accelerator: (a) center cell and (b) end cell with a beam tube. The equator and iris have 1 mm straight sections. Therefore, the shape of the center cell is not entirely the same as that of the TESLA cavity described in [16]. However, the taper angle is adjusted to approximate the TESLA shape.

where k_c is the cell-to-cell coupling, θ is the phase advance between two successive cells, and f_0 is the frequency at 0°. High-impedance HOMs in the passbands correspond to the points of intersection with the light speed line ($v_g = c$) in Fig. 4. The end-cell shape was optimized for the HOM modes with high impedance, such as TE111, TM110, and TM011.

B. Diameter of beam tubes

The diameters of the beam tubes were designed to propagate the HOMs. Damping from one side of the beam

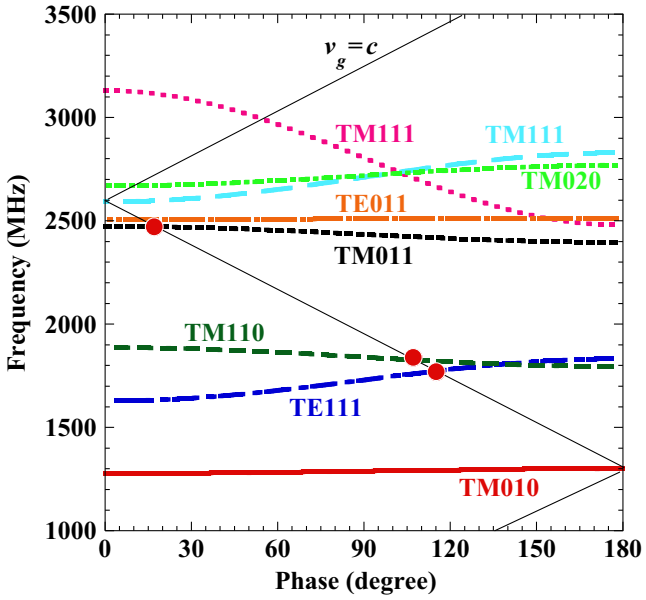

FIG. 4. Dispersion curves of the HOMs in the TESLA-type center cell. The red dots represent the high-impedance HOM modes of TE111, TM110, and TM011. The end-cell frequencies were designed to be tuned to the center-cell frequency for these modes.

TABLE II. Cutoff frequencies of beam tubes of different diameters. The lowest frequencies of the dipole TE111 and monopole TM110 passbands of the center cells were 1627.9 and 1794.0 MHz, respectively. The TE111 passband can be damped via the 110-mm beam tube, and the TM110 passband mode can be damped via both beam tubes.

	Diameter of the beam tubes	Cutoff frequency (MHz)
	TE11	TM01
100 mm (end-cell A)	1756.8	2295.0
110 mm (end-cell B)	1597.1	2086.4

tube for the lowest-order dipole HOMs of the TE111 passband and damping from both sides of the beam tubes for the lowest-order monopole HOMs of the TM110 passband were considered. The lowest frequency of the dipole TE111 passband of the center cells was 1627.9 MHz, whereas that of the monopole TM110 passband of the center cells was 1794.0 MHz. The diameters of both beam tubes were set as 100 and 110 mm. The diameter of 100 mm on one side was chosen to actively make the cavity asymmetric for higher HOM damping. The 100-mm beam pipe can pass from low-order TM110 modes. The cutoff frequencies are listed in Table II. The external Q (Q_{ext}) values corresponded to the coupling between the nine-cell and beam pipes.

C. Design of end cells

The end cell consisted of a TESLA-type center half-cell and end half-cell with a beam tube. The dimensions of the end half-cell were parameterized as shown in Fig. 3(b). A straight section with a width of 1 mm was added for welding at the equator and iris. End-cell A included a 100 mm beam tube, whereas End-cell B included a 110 mm beam tube. The end-cell frequency must be tuned to the high-impedance modes of the center-cell passband. The end cells were strongly coupled with the beam tubes. The end-cell frequency and coupling constant were calculated using the tuning curve method [23,24] (Appendix). This method can be used to calculate only the magnetic boundary modes. Upon applying the calculable modes of the end cell to the dispersion curves of the center cells, it was found that the TE111 mode was 0° whereas the TM010, TM110, and TM011 modes were all 180°. The frequencies of the high-impedance modes cannot be calculated. Because the iris diameter of the end cell on the center cell side is the same as that of the center cell, the slope of the dispersion curve can be assumed to be similar to that of the center cell. Therefore, the optimal shape can be found by sweeping the frequencies of the magnetic boundary modes, as shown in Fig. 5. The frequency differences between the magnetic boundary modes of the center and end cells of TM010, TE111, TM110, and TM011 were defined as $\Delta f_{\mathrm{TM010}}$, $\Delta f_{\mathrm{TE111}}$, $\Delta f_{\mathrm{TM110}}$, and $\Delta f_{\mathrm{TM011}}$, respectively.

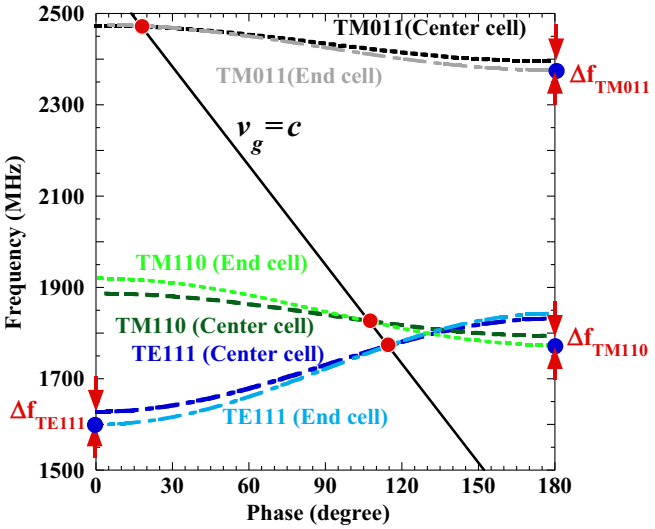

FIG. 5. Conceptual diagram of the optimization of the end-cell frequency. The only calculable HOM modes of the end cell were the magnetic field boundary modes, which are indicated by blue dots on the dispersion curve of the center cell obtained in Fig. 4. The end-cell dispersion curves shown here are conceptual and differ from the actual curves. To optimize the end-cell shape, the dispersion curve of the end cell must be adjusted to match the high-impedance mode of the center cell (red dots). For this purpose, the frequency difference between the magnetic field boundary modes of the HOMs of the center and end cells was defined as $\Delta f_{\mathrm{TE111}}$, $\Delta f_{\mathrm{TM110}}$, and $\Delta f_{\mathrm{TM011}}$, and the optimal shape of the end cells was determined by sweeping this frequency difference.

The accelerating frequency of the end cell was fixed at 1.3 GHz during the optimization process. Because the number of adjustable HOM frequencies was limited by the tolerance of the end-cell shape, two HOM modes were selected for the EUV cavity design. End-cell A was focused on TM110 and TM011, whereas end-cell B was focused on TE111 and TM011. The other HOMs were not controlled. The linearity response terms of the end-cell shape parameters as a function of the HOM frequency and value of Q_{ext} are shown in Table III. The HOM frequencies were adjusted to the target frequency by solving the determinant matrix of the longitudinal axis radius of the iris arc (A_{ir}), longitudinal axis radius of the equator arc (A_{eq}), and transverse axis radius of the equator arc (B_{eq}), with the iris radius (R_{ir}) and cell length (L) as free parameters. R_{ir} and L were swept in 0.25 mm steps. The other shape parameters were fixed because these changes were small. The longitudinal axis radius of the reducer (A_{rd}) was 10 mm, transverse axis radius of the iris arc (B_{ir}) was 14 mm, and transverse axis radius of the reducer arc (B_{rd}) was 5 mm in end-cell A and 8 mm in end-cell B. Because higher-order responses were not included when adjusting the shape, the values of the frequency and Q_{ext} were calculated using the tuning curve method after adjusting the shape.

As mentioned above, only the magnetic boundary modes of the end cells can be calculated, and the frequencies of the magnetic boundary modes were swept to find the optimal end-cell frequency for the high-impedance mode of the nine-cell passband. Three restrictive cavity shape conditions were used for sweeping Δf. First, all sizes were required to be larger than 5 mm for press forming. Second, $(L - A_{\mathrm{ir}} - A_{\mathrm{eq}})$ was required to exceed 0 mm to avoid a reentrant shape. Third, $B_{\mathrm{eq}}\lim_{x\to\infty}$ was required to be larger than 20 mm to avoid a triangular shape. Figure 6 shows the scanning results of the end-cell B shape as an example. The target frequencies of the TM011 mode in the center cell ($\Delta f_{\mathrm{TM011}}$) were adjusted to 0, 5, and 10 MHz. The cavity shapes were adjusted using only linear terms of frequency response. The colored area in the figure indicates the adjustable range for matching the frequencies of the other HOMs (TE111 and TM110) to those of the center cell

TABLE III. Linearity response terms of frequency and Q_{ext} of low-frequency HOMs.

			Frequency response (MHz/mm)				Q_{ext} response (mm^{-1})		
Dimension		Initial length (mm)	TM010	TE111	TM110	TM011	TE111	TM110	TM011
End-cell A	A_{ir}	11	−1.71	4.63	−0.89	5.28	NA	0.65	8.05
	A_{eq}	37.49	−3.39	−1.97	−1.87	−14.49	NA	−1.80	6.20
	B_{ir}	14	0.42	−1.20	0.08	−1.01	NA	0.14	−1.92
	B_{eq}	40	1.13	0.46	0.84	3.57	NA	−0.12	−2.04
	R_{ir}	39	1.57	−8.10	−4.44	−1.63	NA	−3.63	−20.61
	L	53	2.12	−5.38	1.40	−5.53	NA	3.64	−4.37
End-cell B	A_{ir}	12	−1.74	5.50	−0.90	4.61	−0.17	−0.50	11.46
	A_{eq}	37.54	−3.38	−1.93	−1.72	−14.54	3.10	−2.07	6.26
	B_{ir}	14	0.45	−1.52	0.07	−0.82	−0.23	0.13	−2.84
	B_{eq}	40	1.14	0.45	0.80	3.64	−0.78	0.57	−2.38
	R_{ir}	39	1.58	−11.31	−4.07	0.06	−26.74	−5.99	−27.88
	L	54	2.12	−5.83	1.26	−5.07	5.57	3.81	−6.52

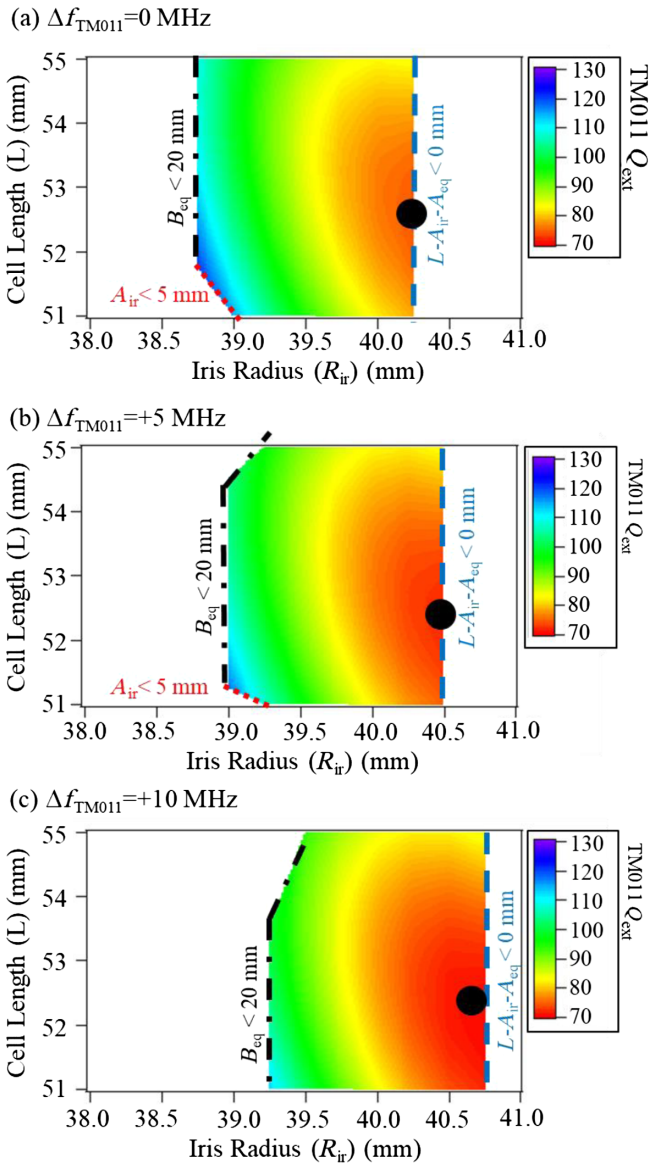

FIG. 6. Example of the scanning results of end-cell B shape. The color scale shows Q_{ext} of TM011. The calculation conditions were (a) $\Delta f_{TM011} = 0$ MHz, (b) $\Delta f_{TM011} = 5$ MHz, and (c) $\Delta f_{TM011} = 10$ MHz with $\Delta f_{TM010} = 0$ MHz, $\Delta f_{TE111} = 0$ MHz, and $\Delta f_{TM110} = 0$ MHz. The dashed lines denote the restricted conditions. The red dashed lines show the conditions at which A_{ir} is larger than 5 mm for press forming. The blue dashed lines show the conditions in which $(L - A_{ir} - A_{eq})$ is larger than 0 mm to avoid a reentrant shape. The black dashed lines show the conditions where B_{eq} is larger than 20 mm to avoid a triangular shape. The coloring gradient shows the Q_{ext} values of the TM011 mode. The values denoted by black dots, which were obtained with the minimum Q_{ext}, were selected as the optimal values.

($\Delta f_{TE111} = 0$ MHz and $\Delta f_{TM110} = 0$ MHz). The color scales indicate the values of Q_{ext} for the TM011 mode. The shapes with the lowest values of Q_{ext} were selected as candidates for optimization. After selecting the candidate cavity shape, the actual frequency difference was calculated. Then, the target frequency of the end cell was swept to determine the optimal shape.

IV. OPTIMIZATION OF CAVITY SHAPE

The optimal cavity shape for an EUV cavity was selected by combining seven center cells and two end cells and calculating the shunt impedance of a nine-cell cavity. The targets for optimization were TE111, TM110, and TM011, and each mode was investigated separately. The end cells were adjusted to determine the minimum shunt impedance for each mode. The conditions for adjusting each mode are shown in Table IV. In all cases, each end cell was adjusted to the accelerating frequency and two HOM frequencies. The value of Q_{ext} of the nine-cell cavity was calculated using the CST-MW studio.

Case 1: The target mode in case 1 was TE111. The minimum shunt impedance of TE111 was determined by sweeping Δf_{TE111} of end-cell B. Δf_{TM110} of end-cell A and Δf_{TM011} of both end cells were adjusted to zero. Figure 7 shows the shunt impedance of TE111, which was swept from -27.3 to $+19$ MHz with steps of approximately 5 MHz. The highest impedance of the TE111 mode was $6\pi/9$. The difference was negligible when the end-cell frequency was varied, and the transverse shunt impedance was lower than 4×10^3 in all cases.

Case 2: The target mode in case 2 was TM110, which was optimized in a similar manner as that in case-1. The minimum shunt impedance of TM110 was determined by changing Δf_{TM110} of end-cell A under the conditions that Δf_{TM110} of both end cells and Δf_{TE111} of end-cell A were set to zero. Figure 8 shows the shunt impedance of TM110, which was swept from -16.1 to $+20$ MHz with steps of approximately 5 MHz. The highest impedance of the TM110 passband was $5\pi/9$. The difference was negligible when the end-cell frequency was varied, and the transverse shunt impedance was lower than 2×10^4 in all cases.

Case 3: The difference between the best values of both TE111 and TM110 was small. Therefore, both end-cell frequencies were optimized to the high-impedance mode in the TM011 $\pi/9$ mode. Figure 9(a) shows the shunt impedance of the nine-cell TM011 as a function of various Δf_{TM011} values for both end cells, where Δf_{TM110} of end-cell A and Δf_{TE111} of end-cell B were fixed to zero. The highest impedance mode of TM011 was observed in the $\pi/9$ mode. Figure 9(b) shows the $\pi/9$ TM011 mode in greater detail. The minimum shunt impedance $(R/Q \times Q_{ext})$ was 5×10^4 Ω when Δf_{TM011} of end-cell A and B was $+8.2$ and $+3.8$ MHz, respectively. These end-cell shapes were selected for the optimized EUV nine-cell cavity. The fabrication error of the cavity was approximately 0.1 mm, and the frequency varied by up to approximately 1 MHz from the frequency response of the end cell for each dimension, as shown in Table III.

The optimized dimensions of both end-cell shapes are listed in Table V. The parameters of the accelerating mode

TABLE IV. Evaluation range for HOM optimization of the EUV nine-cell cavity.

	End-cell A		End-cell B	
Target HOM mode	$\Delta f_{\mathrm{TM110}}$	$\Delta f_{\mathrm{TM011}}$	$\Delta f_{\mathrm{TE111}}$	$\Delta f_{\mathrm{TM011}}$
Case-1 TE111	0 MHz	0 MHz	−27.3 MHz to +19 MHz	0 MHz
Case-2 TM110	−16.1 MHz to +20 MHz	0 MHz	0 MHz	0 MHz
Case-3 TM011	0 MHz	−21 MHz to +18.8 MHz	0 MHz	−1.3 MHz to +20.3 MHz

in the EUV nine-cell cavity were calculated using SUPERFISH. A comparison with the TESLA cavity is listed in Table VI. The $E_{\mathrm{sp}}/E_{\mathrm{acc}}$ value of the EUV cavity was almost identical to that of the TESLA cavity and met the target value of 2.0. Figure 10 shows the calculation results of the HOM impedance in the EUV nine-cell cavity. The monopole modes with the highest shunt impedance of TM011 and TM020 were $5.0 \times 10^4\ \Omega$ at 2469 MHz and $3.6 \times 10^4\ \Omega$ at 2664 MHz, respectively. The monopole-mode power loss under the condition of the beam repetition matching the HOM frequencies was 19 W, as calculated using Eq. (1); however, this was unlikely to happen because the beam repetition and HOM frequencies were adequately spaced. The dipole modes with the highest transverse shunt impedance of TE111 and TM110 were $3.4 \times 10^3\ \Omega\,\mathrm{cm}^{-1}\,\mathrm{GHz}^{-1}$ at 1730 MHz and $3.1 \times 10^4\ \Omega\,\mathrm{cm}^{-1}\,\mathrm{GHz}^{-1}$ at 1874 MHz, respectively. The highest transverse shunt impedances of TE111 and TM110 for the ERL model 1 cavity were 2.7×10^4 at 1866 MHz and 5.5×10^4 at 1874 MHz, respectively [3]. The dipole-mode impedances of the EUV cavity were lower than the target value, and the BBU threshold was sufficiently satisfied.

Figure 11 shows the loss factor of the EUV cavity calculated with echo [25]. The loss factor in the EUV cavity was slightly higher than that of the TESLA cavity because the EUV cavity incorporates the reducer part extending from the end cells to the beam tubes [26]. The total power losses in one cavity with the EUV parameters of bunch width of 1 or 2 ps in rms, bunch charge of 60 pC, and bunch repetition of 325 MHz were 34 W (1 ps) and 23 W (2 ps). Considering that one HOM damper is used between the two cavities, the absorbed power at the HOM damper was approximately 34 W (1 ps) and 23 W (2 ps) on average.

V. OPTIMIZATION OF HOM DAMPER

A single cryomodule for the EUV accelerator contains four or eight nine-cell cavities. Each nine-cell cavity is connected with an HOM damper. Many types of rf damping materials are used for HOM dampers in SRF accelerators. Aluminum nitride (Model STL-150D) supplied by Sienna Technologies Inc., USA [27], was used for its capability to maintain the rf damping characteristics even at cryogenic temperatures. The same material was used at CEBAF [28] and Euro XFEL [29]. The rf characteristics of the material

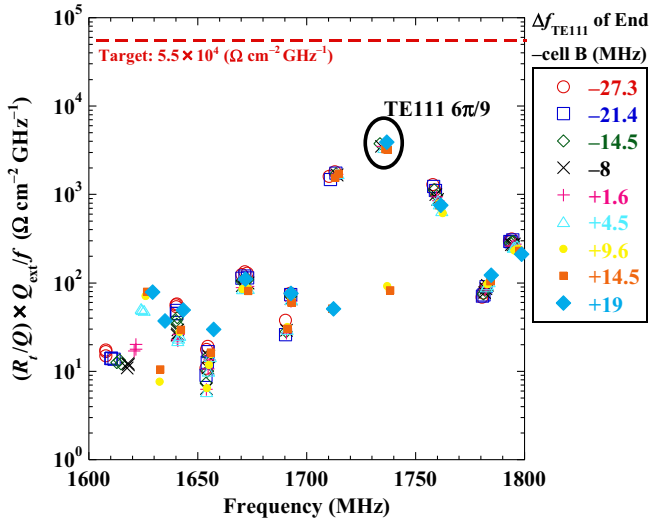

FIG. 7. Impedance of TE111 passband mode. The $\Delta f_{\mathrm{TE111}}$ value of end-cell B was swept from −27.3 to +19 MHz with steps of approximately 5 MHz under the condition that $\Delta f_{\mathrm{TM110}}$ of end-cell A and $\Delta f_{\mathrm{TM011}}$ of both end cells were set to zero.

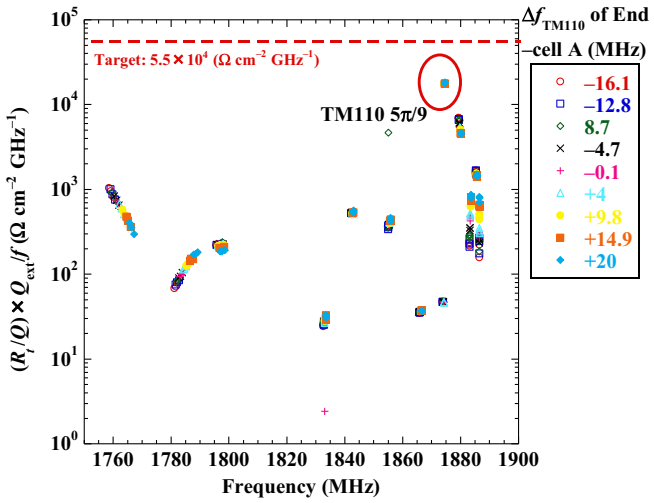

FIG. 8. Impedance of TM110 passband mode. $\Delta f_{\mathrm{TM110}}$ of end-cell B was swept from −16.1 to +20 MHz with steps of approximately 5 MHz under the condition that $\Delta f_{\mathrm{TM110}}$ of both end cells and $\Delta f_{\mathrm{TE111}}$ of end-cell A were set to zero.

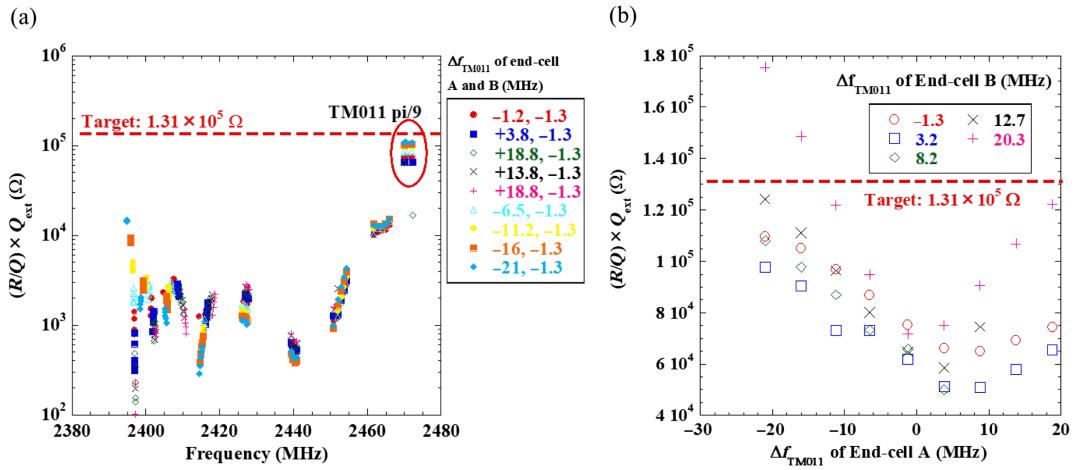

FIG. 9. Shunt impedance of the TM011 mode with various end-cell frequencies. (a) All TM011 HOM spectra; the first and second values in the legend are the $\Delta f_{\mathrm{TM011}}$ values of end-cells A and B, respectively. (b) The detailed TM011 $\pi/9$ mode. The legend shows $\Delta f_{\mathrm{TM011}}$ of end-cell B. The minimum shunt impedance is $5 \times 10^4 \Omega$ when $\Delta f_{\mathrm{TM011}}$ of end-cell A is +8.2 and end-cell B is +3.8 MHz.

were measured at 300 and 80 K using the complex permittivity obtained with the transmission/reflection method in the coaxial line [30–32]. Figure 12 shows the measurement results of the permittivity of the material in a liquid nitrogen bath at KEK [33]. The data were fitted using a Debye second-order model and used for the HOM damper design [34].

$$\epsilon(\omega) = \epsilon_\infty + \frac{\epsilon_s - \epsilon_\infty}{1 + i\omega t} \cong \left(1 + \frac{\epsilon_1}{1 + (\omega/\omega_1)^2} + \frac{\epsilon_2}{1 + (\omega/\omega_2)^2}\right) + \mathrm{j}\left(\frac{\epsilon_1 \cdot \omega/\omega_1}{1 + (\omega/\omega_1)^2} + \frac{\epsilon_2 \cdot \omega/\omega_2}{1 + (\omega/\omega_2)^2}\right) \quad (5)$$

where ϵ_1 and ϵ_2 are the initial relative permittivities, and ω_1 and ω_2 are the relaxation frequencies. The permeability was constant at 1.0.

The structure of the HOM damper [Fig. 13(a)] was designed considering the data obtained at 80 K. It was designed to operate with a heat load of more than 100 W considering the measurement results and the reliable brazing method. The damper was connected to a thin copper tube with a silver–copper brazing compound and was thermally intercepted at 80 K. The flanges at both ends were connected with the thermal anchors at 5 K. A bellows of 0.15 mm thickness was used to connect the copper tube with the flange to suppress the heat flow from 80 to 5 K. The prototype HOM damper was tested in a cryostat with a 10 W heater [35]. The measured heat distribution was as designed. Although a further detailed study is needed, we assumed that heat generation of approximately 100 W could be adequately damped.

The actual loss on the HOM damper was mainly caused by the loss factor. Figure 13(b) shows the static simulation of the HOM damper. When the heat inflow to the HOM damper was 100 W in the static simulations, the damper temperature increased to 96 K. The loss factor around 96 K was not measured. Because dielectric losses are greater at higher temperatures, the damper is expected to maintain below 96 K.

The optimal dimensions of the damper are summarized as follows: The distance from the end-cell cavity to the HOM damper was designed such that the rf loss of the cavity accelerating mode was less than 1% of the cavity wall loss. Figure 14 shows the schematic structure of the EUV cavity with the HOM damper. The distance between

TABLE V. Optimized dimensions (mm) of end-cells A and B.

Parameter	Symbol	End-cell A	End-cell B
Long. iris arc	A_{ir}	8.97	9.98
Trans. iris arc	B_{ir}	14.00	14.00
Iris radius	R_{ir}	39.75	40.75
Long. equator arc	A_{eq}	38.90	41.33
Trans. equator arc	B_{eq}	42.00	49.49
Equator radius	R_{eq}	103.30	103.30
Long. reducer	A_{rd}	10.00	10.00
Trans. reducer	B_{rd}	5.00	8.00
Beam-tube radius	R_{bp}	50.00	55.00
End half-cell length	L	52.00	52.00

TABLE VI. Comparison of the main parameters of the EUV and TESLA nine-cell cavities.

Cavity parameter	EUV	TESLA [16]
Frequency (MHz)	1300	1300
Iris diameter (mm)	70	70
Beam-tube diameter (mm)	100/110	78/78
R/Q (Ω)	1009	1036
G (Ω)	269	270
$E_{\mathrm{sp}}/E_{\mathrm{acc}}$	2.0	2.0
$H_{\mathrm{sp}}/E_{\mathrm{acc}}$ [mT/(MV/m)]	4.23	4.26

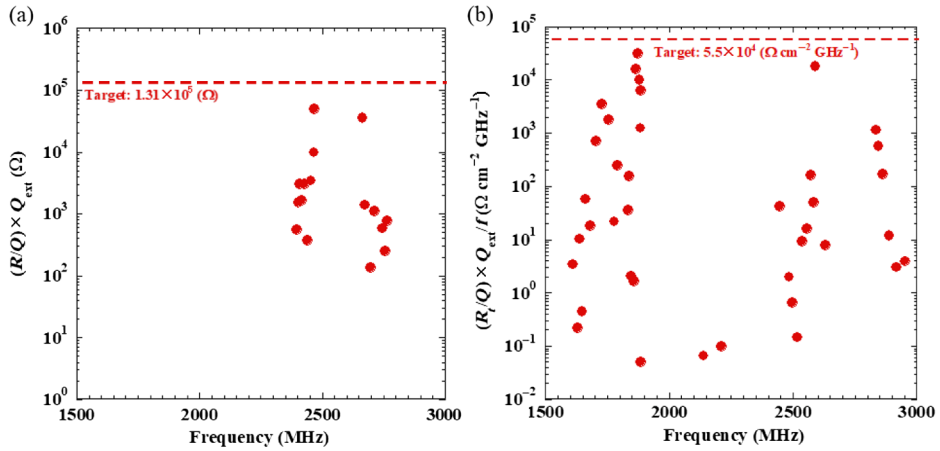

FIG. 10. HOM impedance spectrum in the optimized EUV nine-cell cavity. (a) Shunt impedance of the monopole HOMs. No HOM lower than 2397 MHz was present. The mode with the highest shunt impedance of TM011 was 5.0×10^4 Ω at 2469 MHz. The mode with the highest shunt impedance of TM020 was 3.6×10^4 Ω at 2664 MHz. (b) Transverse shunt impedance of dipole HOMs. The mode with the highest transverse shunt impedance of TE111 was 3.4×10^3 $\Omega\,\mathrm{cm}^{-1}\,\mathrm{GHz}^{-1}$ at 1730 MHz. The mode with the highest transverse shunt impedance of TM110 was 3.1×10^4 $\Omega\,\mathrm{cm}^{-1}\,\mathrm{GHz}^{-1}$ at 1874 MHz. The other mode with the highest impedance at approximately 2590 MHz was trapped by the cavity iris. The shunt impedance of the iris mode was 1.8×10^4 $\Omega\,\mathrm{cm}^{-1}\,\mathrm{GHz}^{-1}$.

the stainless-steel pipe and the end iris of the beam tube of ϕ100 mm in the cavity was 127 mm. The distance between the damper and the cavity was 280 mm. The distance between the stainless-steel pipe and the end iris of the beam tube of ϕ110 mm in the cavity was 182 mm. The distance between the damper and the cavity was 290 mm. An rf absorber length of 100 mm, inner diameter of 100 mm, and thickness of 10 mm are required to cover all HOM frequencies.

The damper power absorptions for the TM and TE modes were evaluated based on the transmitted rf loss, as shown in Fig. 15. The TM and TE modes can consume approximately 80% and 60% of the total power, respectively, although these values gradually decrease at higher frequencies.

HOM damper shape and material properties were inputted to simulate HOM parameters. The HOM damper

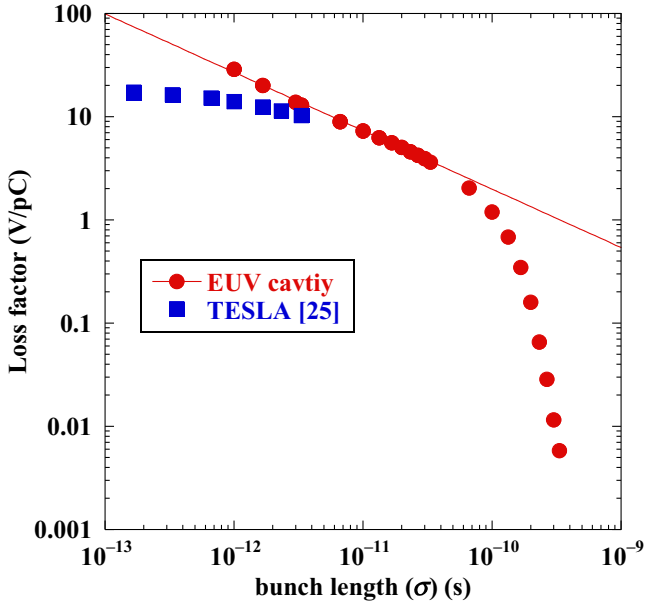

FIG. 11. Loss factor of the EUV nine-cell cavity as a function of the beam bunch length. The curve was fitted between 30 and 1 ps, which was adequately shorter than the cell length. The fitting value was $4.3 \times 10^{-6} \times \sigma^{-0.57}$, where σ is the bunch length in rms. The loss factor of the TESLA cavity is presented in [26].

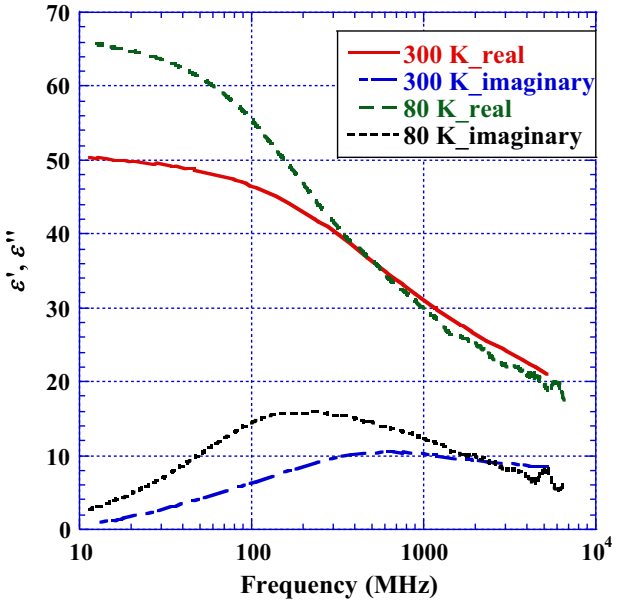

FIG. 12. Relative permittivity of aluminum nitride (STL-150D, Sienna Technologies Inc.) measured at room temperature (300 K) and in liquid nitrogen (80 K) as a function of the measured frequencies from 10 MHz to 6 GHz. The 80 K data were fitted using a Debye second-order model for designing the HOM damper [33]. The permeability of the HOM damper was 1.0.

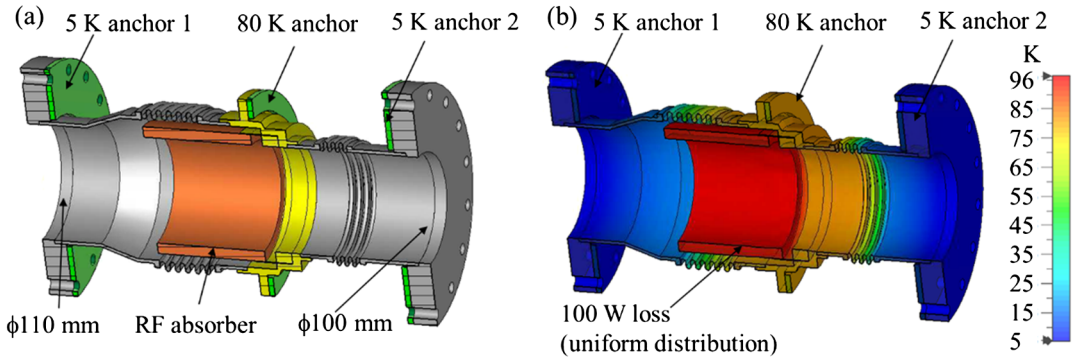

FIG. 13. Design of the prototype HOM damper. (a) Diameters of the beam tubes are 110 mm on the left-hand side and 100 mm on the right-hand side, and the tubes are directly joined with the EUV nine-cell cavity. Gray parts indicate stainless steel, yellow parts indicate RRR300 copper, orange part indicates aluminum nitride, and green parts indicate thermal anchors. All parts were connected without thermal contact resistance. The actual structure of the thermal anchors was copper blocks brazed with copper cooling tubes and mounted on flanges with bolts. (b) Results of thermal simulation. The thermal radiation effect is not included. With an input of 100 W, the heat flows to 5-K anchor 1, 5-K anchor 2, and 80-K anchor are −0.175, −0.28, and −99.6 W, respectively. Without the input of 100 W, the heat flows to 5-K anchor 1, 5-K anchor 2, and 80-K anchor are −0.16, −0.28, and 0.41 W, respectively.

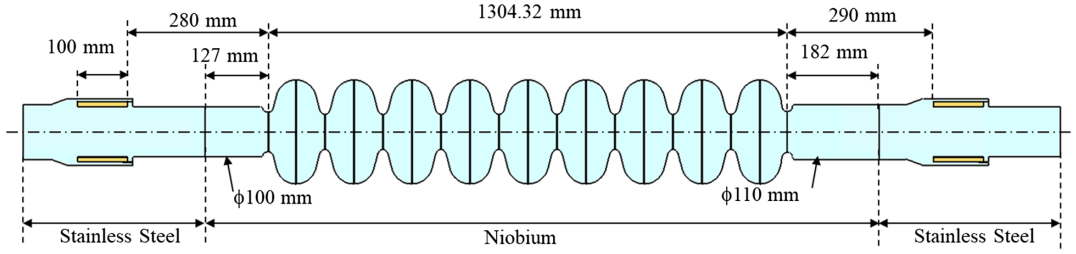

FIG. 14. Structure of the EUV cavity with the HOM damper. The rf losses in the stainless-steel pipe and HOM damper were designed to be less than 1% of the acceleration mode. The HOM damper and cavity are connected in the same direction in sequence.

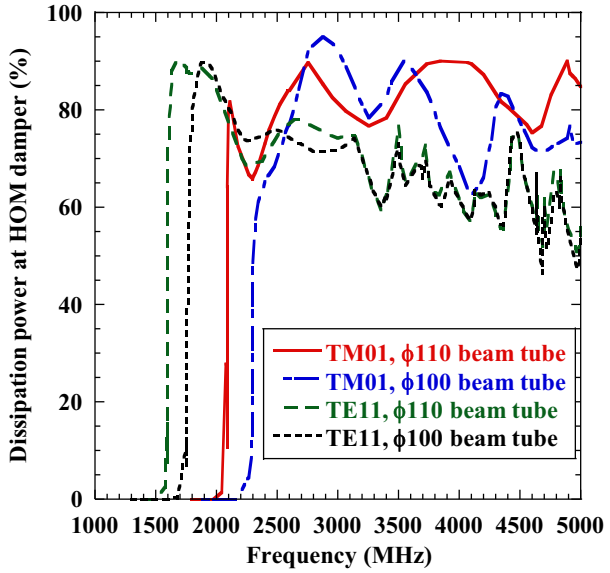

FIG. 15. Calculation results for propagation and absorption of HOM power at the HOM damper. The rf powers of the TM01 and TE11 modes were transferred from the Φ110 mm or Φ100 mm beam tube.

material data were fitted data shown in Fig. 13 with the Debye second-order model. The shunt impedances of the monopole and dipole HOMs are shown in Fig. 16. The shunt impedance was evaluated using the loaded Q value (Q_{Load}), which was damped on both sides of the HOM damper. Q_{Load} and the frequency were not the same as those in the simulation conducted without a damper because the field leaked into the beam tube. The beam repetition and HOM frequencies were adequately different from one another. The monopole mode with the highest shunt impedance of TM011 was $1.2 \times 10^5\ \Omega$ at 2469 MHz. The maximum shunt impedance of the monopole was approximately 2 times higher, which was within the assumptions of the HOM damper design. The beam repetition frequency and harmonics were adequately far from the frequency of the high-impedance HOM. Although unlikely, if the beam repetition and HOM frequencies are matched, the total heat generation at both HOM dampers would be approximately 43 W according to Eq. (1). The dipole mode with the highest transverse shunt impedance of TM110 was $2.6 \times 10^4\ \Omega\,\mathrm{cm}^{-2}\,\mathrm{GHz}^{-1}$ at 1874 MHz, which is smaller than reference ERL model 1 shunt impedance $5.5 \times 10^4\ \Omega\,\mathrm{cm}^{-2}\,\mathrm{GHz}^{-1}$ at 1874 MHz [3]. The dipole

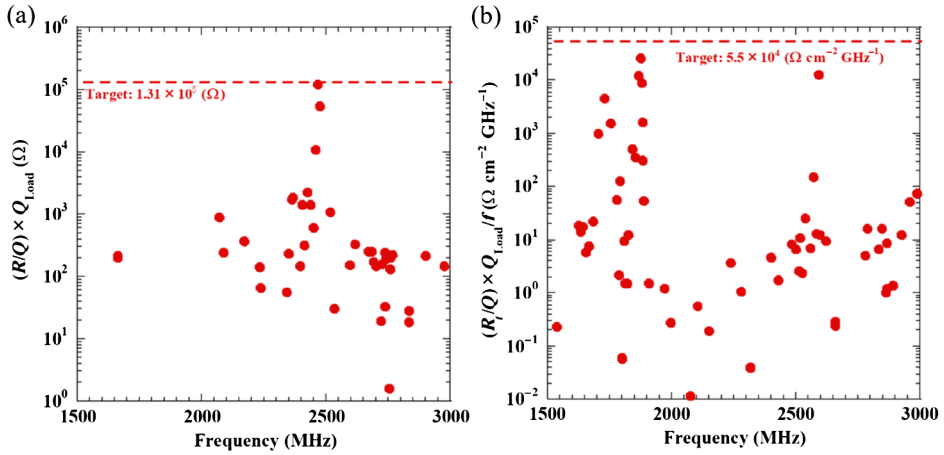

FIG. 16. HOM impedance spectra in the EUV nine-cell cavity with the HOM damper. The cavity with HOM damper shape is shown in Fig. 15. The permittivity of HOM damper material was inputted fitted data of 80 K measurement data in Fig. 13 by the Debye second-order model. (a) Monopole modes in which modes around 1660 MHz were trapped at the HOM damper. The mode with the highest shunt impedance of TM011 was $1.2 \times 10^5\ \Omega$ at 2469 MHz. This was approximately 2 times higher than the HOM simulation without the damper, as shown in Fig. 11(a). (b) Dipole modes. The mode with the highest transverse shunt impedance of TM110 was $2.6 \times 10^4\ \Omega\,\mathrm{cm}^{-2}\,\mathrm{GHz}^{-1}$ at 1874 MHz.

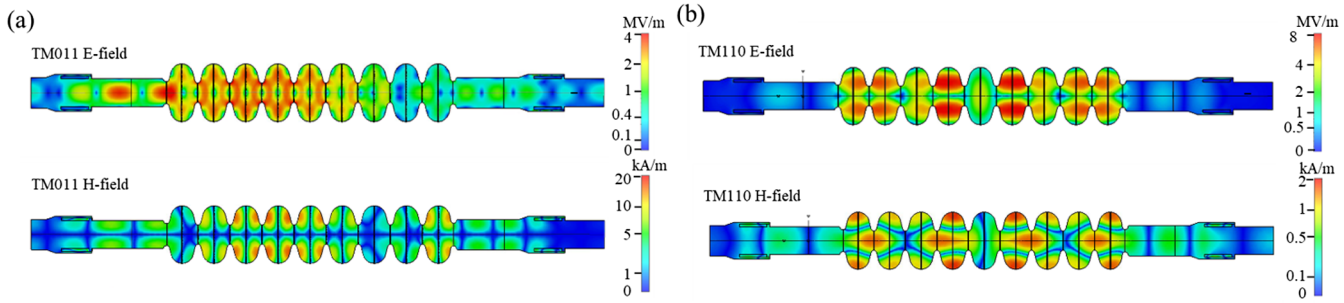

FIG. 17. High-impedance HOM electric and magnetic field distributions. The field strength is shown using a logarithmic scale. (a) Monopole high-impedance mode of 2469 MHz in TM011. This field can propagate to the HOM dampers, but the shunt impedance is relatively high due to the high R/Q value. (b) Dipole high-impedance mode of 1874 MHz in TM110. This field was trapped in the cells. Although the field propagated to the HOM dampers was small, the shunt impedance was sufficiently lower than the target value.

mode was lower than that in the simulation without the HOM damper. The field distributions of the high-impedance monopole and dipole HOMs are shown in Fig. 17. The BBU target was adequately satisfied.

VI. CONCLUSION

A nine-cell superconducting cavity with a HOM damper was designed to realize stable operation for the 10-mA-class EUV-FEL accelerator. The center-cell shape was selected to set $E_{\mathrm{sp}}/E_{\mathrm{acc}}$ of 2.0 for stable operation without field emission. The end-cell shape was designed by prioritizing the minimization of the impedance of the monopole TM011 mode because the difference in the case of the other dipole modes was small. The highest shunt impedances of TM011 were $1.2 \times 10^5\ \Omega$ and $5.0 \times 10^4\ \Omega$ with and without the HOM damper, respectively. The beam repetition frequency and high-impedance HOM were adequately far from each other. Although unlikely, even if the beam repetition and HOM frequencies match, the total heat generation at both HOM dampers would be approximately 43 W. The average power losses estimated from the loss factor were 34 and 23 W for bunch lengths of 1 and 2 ps in rms, respectively. Consequently, the thermal structure for the HOM damper requires power of more than 50 W. Developing a HOM damper that can absorb power of 100 W will provide sufficient margin for operation. The highest transverse shunt impedance of the TM110 mode with the HOM damper was $2.6 \times 10^4\ \Omega\,\mathrm{cm}^{-2}\,\mathrm{GHz}^{-1}$ at 1874 MHz, which was adequately lower than the target impedance of $5.0 \times 10^5\ \Omega\,\mathrm{cm}^{-2}\,\mathrm{GHz}^{-1}$. Therefore, a sufficient margin is present for BBU of the EUV-FEL accelerator. Thus, the designed EUV nine-cell cavity with HOM dampers has a suitable margin for the 10-mA-class EUV-FEL accelerator.

APPENDIX: IDENTIFICATION OF END-CELL RESONANT FREQUENCY USING THE TUNING CURVE METHOD

The end cell is strongly coupled with the beam tube, and identifying the resonant frequency using the tuning curve method is necessary [22,23]. The tuning curve can be used to determine the end-cell resonant frequency and coupling between the end cell and beam tube by calculating the eigenmode frequencies while varying the length of the beam tube. Figure 18 shows an example of the tuning curve method using end-cell A. The eigenmode frequencies of end-cell A were calculated with different beam-tube lengths. The frequency of the end cell is constant along the vertical lines. The beam-tube frequency is shown by the curve tangential to the cutoff frequency line. The coupling between the end cell and beam tube was calculated from the curvature of the intersection of the cell frequency line and beam-tube frequency. These calculations were performed using the following equation:

$$L_{\mathrm{bp}} = \frac{1000}{\sqrt{(2\pi f)^2 - (j_{mn}/R_{\mathrm{bp}})^2}} \left\{ \pi \left[n + \mathrm{int}\left(\frac{f_0}{f}\right) \right] + \tan^{-1}\left(\frac{1}{Q_{\mathrm{ext}}(f/f_0 - f_0/f)} \right) \right\} - L_{\mathrm{boundary}}, \quad \text{(A1)}$$

where L_{bp} is the beam-tube length, j_{mn} is a Bessel function, Q_{ext} denotes the coupling of the beam tube and end cell, f_0 is the end-cell frequency, n is an integer corresponding to the beam-tube wave node, R_{bp} is the beam-tube radius, and L_{boundary} is the distance from the end-cell iris to the imaginary short plane, which is a magnetic boundary. Therefore, only the magnetic boundary modes of the end cell can be calculated.

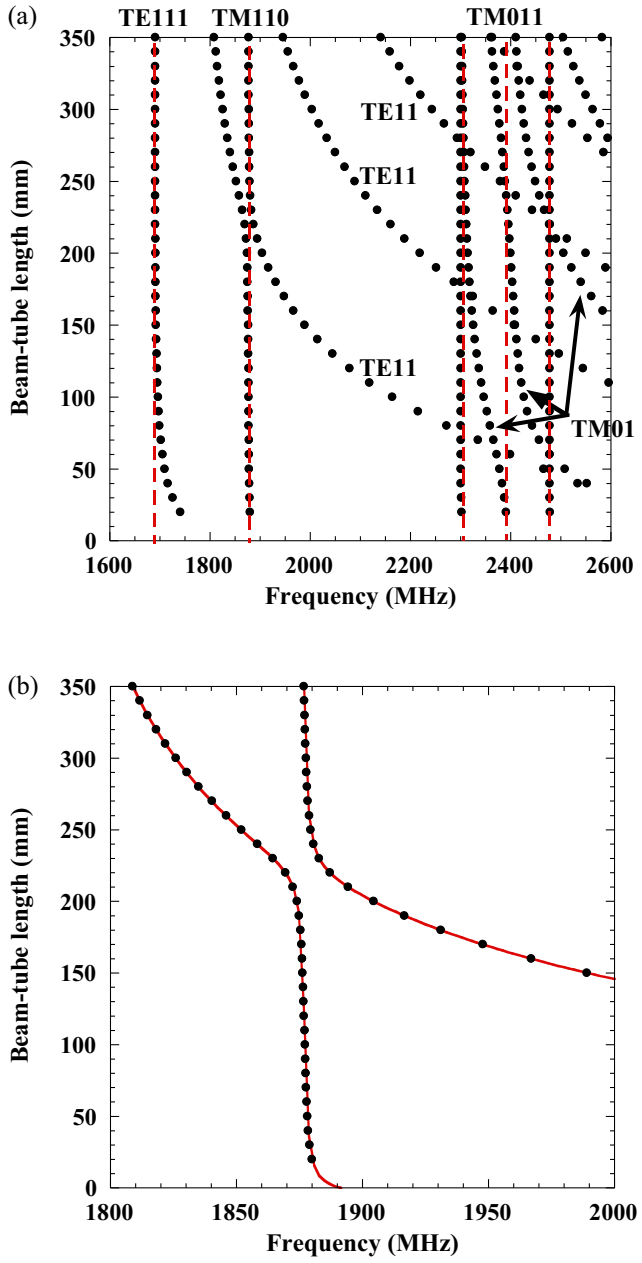

FIG. 18. Example of the tuning curve method. The calculation results of the tuning curve are shown for the beam-tube length vs frequency in the ranges of (a) 1600–2600 MHz and (b) 1800–2000 MHz. The vertical red dashed lines show the cavity resonant frequencies. The curves across the vertical lines show the beam-tube modes. The coupling (Q_{ext}) between the end cell and beam tubes was calculated from the curvature of the intersection using Eq. (3).

[1] E. R. Hosler, O. R. Wood II, and M. E. Preil, Extending extreme-UV lithography technology, in *SPIE Newsroom* (SPIE, Bellingham, Washington, DC, 2016), 10.1117/2.1201601.006323.

[2] R. Kato, H. Sakai, K. Tsuchiya, Y. Tanimoto, Y. Honda, T. Miyajima, M. Shimada, N. Nakamura, and H. Kawata, Stepwise development to realize the high power EUV-FEL light source, in *OSA High-brightness Sources and Light-driven Interactions Congress 2020 (EUVXRAY, HILAS, MICS), Washington, DC, USA, 2020* (Optical Society of America, Massachusetts Ave. NW, Washington, DC, 2020), paper Eth2A.2, https://opg.optica.org/abstract.cfm?URI=EUVXRAY-2020-ETh2A.2.

[3] N. Nakamura *et al.*, Design work of the ERL-FEL as the high intense EUV light source, in *Proceedings of ERL2015, Stony Brook, NY, 2015* (JACoW, Geneva, Switzerland, 2015), pp. 4–9, 10.18429/JACoW-ERL2015-MOPCTH010.

[4] H. Sakai, E. Kako, T. Konomi, T. Kubo, K. Umemori, T. Ota, and M. Sawamura, Superconducting accelerator for ERL based FEL EUV light source at KEK, in *Proceedings of the 18th International Conference on RF Superconductivity (SRF'17), Lanzhou, China, 2017* (JACoW, Geneva, Switzerland, 2017), pp. 13–18, 10.18429/JACoW-SRF2017-MOXA04.

[5] H. Kawata, N. Nakamura, H. Sakai, R. Kato, and R. Hajima, High power light source for future extreme

ultraviolet lithography based on energy-recovery linac free-electron laser, J. Micro/Nanopatterning, Mater., Metrol. **21**, 021210 (2022).

[6] M. Tigner, A possible apparatus for electron clashing-beam experiments, Nuovo Cimento (1955–1965) **37**, 1228 (1965).

[7] T. I. Smith, H. A. Schwettman, R. Rohatgi, Y. Lapierre, and J. Edighoffer, Development of the SCA/FEL for use in biomedical and materials science experiments, Nucl. Instrum. Methods Phys. Res., Sect. A **259**, 1 (1987).

[8] G. R. Neil, C. L. Bohn, S. V. Benson, G. Biallas, D. Douglas, H. F. Dylla, R. Evans, J. Fugitt, A. Grippo, J. Gubeli, R. Hill, K. Jordan, R. Li, L. Merminga, P. Piot, J. Preble, M. Shinn, T. Siggins, R. Walker, and B. Yunn, Sustained kilowatt lasing in a free-electron laser with same-cell energy recovery, Phys. Rev. Lett. **84**, 662 (2000).

[9] I. V. Bazarov, Overview of energy recovery linacs, in *Proceedings of the 21st Particle Accelerator Conference, Knoxville, TN, 2005* (IEEE, Piscataway, NJ, 2005), pp. 382–386, https://accelconf.web.cern.ch/p05/PAPERS/TOPB004.PDF.

[10] M. Akemoto *et al.*, Construction and commissioning of the compact energy-recovery linac at KEK, Nucl. Instrum. Methods Phys. Res., Sect. A **877**, 197 (2018).

[11] H. Sakai, E. Cenni, K. Enami, T. Furuya, M. Sawamura, K. Shinoe, and K. Umemori, Field emission studies in vertical test and during cryomodule operation using precise x-ray mapping system, Phys. Rev. Accel. Beams **22**, 022002 (2019).

[12] A. Neumann, J. Knobloch, K. Brackebusch, T. Flisgen, T. Galek, U. van Rienen, B. Riemann, and T. Weis, Final design for the BERLinPro main linac cavity, in *Proceedings of LINAC2014, Geneva, Switzerland* (JACoW, Geneva, Switzerland, 2014), pp. 217–220, 10.13140/2.1.1313.8722.

[13] N. Valles, M. Liepe, F. Furuta, M. Gi, D. Gonnella, Y. He, K. Ho, G. Hoffstaetter, D. S. Klein, T. O'Connell, S. Posen, P. Quigley, J. Sears, G. Q. Stedman, M. Tigner, and V. Veshcherevich, The main linac cavity for Cornell's energy recovery linac: Cavity design through horizontal cryomodule prototype test, Nucl. Instrum. Methods Phys. Res., Sect. A **734**, 23 (2014).

[14] C. Xu, I. Ben-Zvi, Y. Hao, T. Xin, and H. Wang, Conceptual design of a high real-estate gradient cavity for a SRF ERL, Nucl. Instrum. Methods Phys. Res., Sect. A **869**, 128 (2017).

[15] M. Sawamura, T. Furuya, H. Sakai, T. Takahashi, K. Umemori, and K. Shinoe, Eccentric-fluted beam pipes to damp quadrupole higher-order modes, Phys. Rev. ST Accel. Beams **13**, 022003 (2010).

[16] B. Aune *et al.*, Superconducting TESLA cavities, Phys. Rev. ST Accel. Beams **3**, 092001 (2000).

[17] H. Padamsee, J. Knobloch, and T. Hays, *RF Superconductivity forAccelerators* (Wiley, New York, 1998), p. 523, ISBN 978-3-527-40842-9.

[18] K. Umemori, T. Furuya, S. Sakanaka, T. Suwada, T. Takahashi, H. Sakai, K. Shinoe, and M. Sawamura, Design of L-band superconducting cavity for the energy recovery linacs, in *Proceedings of the 4th Asian Particle Accelerator Conference, Indore, India* (RRCAT, Indore, India, 2007), pp. 570–572, https://accelconf.web.cern.ch/a07/PAPERS/THC2MA03.PDF.

[19] H. Sakai, K. Shinoe, T. Furuya, S. Sakanaka, T. Suwada, T. Takahashi, K. Umemori, and M. Sawamura, Development of a 1.3 GHz 9-cell superconducting cavity for the energy recovery linac, in *Proceedings of 41st Advanced ICFA Beam Dynamics Workshop on Energy Recovery Linacs, ERL07, Daresbury, UK* (JACoW, Geneva, Switzerland, 2007), pp. 56–61, http://accelconf.web.cern.ch/erl07/papers/34.pdf.

[20] M. Liepe, Conceptual layout of the cavity string of the Cornell ERL main linac cryomodule, in *Proceedings of the 11th Workshop on RF Superconductivity (SRF2003), Lübeck/Travemünder, Germany* (JACoW, Geneva, 2003), pp. 115–119, https://accelconf.web.cern.ch/SRF2003/papers/mop33.pdf.

[21] E. Pozdeyev, C. Tennant, J. J. Bisognano, M. Sawamura, R. Hajima, and T. I. Smith, Multipass beam breakup in energy recovery linacs, Nucl. Instrum. Methods Phys. Res., Sect. A **557**, 176 (2006).

[22] Dassault systems, CST Studio, https://www.3ds.com/.

[23] J. C. Slater, Microwave electronics, Rev. Mod. Phys. **18**, 441 (1946).

[24] T. Kageyama, A simple method using MAFIA to calculate external Q values of waveguide-loaded cavities, KEK Report No. 89-4, 1989, https://inis.iaea.org/collection/NCLCollectionStore/_Public/21/024/21024292.pdf.

[25] I. Zagorodnov and T. Weiland, TE/TM field solver for particle beam simulations without numerical Cherenkov radiation, Phys. Rev. ST Accel. Beams **8**, 042001 (2005).

[26] Alexandre Novokhatski and Alban Mosnier, Short bunch wake potentials for a chain of TESLA cavities, Nucl. Instrum. Methods Phys. Res., Sect. A **763**, 202 (2014).

[27] SIENNA TECHNOLOGIES Inc., https://siennatech.com/.

[28] F. Marhauser, T. Elliot, A. T. Wu, E. Savrun, and E. Chojnacki, Absorber materials at room and cryogenic temperatures, in *Proceedings of the 2nd International Particle Accelerator Conference, IPAC-2011, San Sebastián, Spain* (EPS-AG, Spain, 2011), pp. 1792–1794, https://accelconf.web.cern.ch/IPAC2011/papers/tups106.pdf.

[29] J. Sekutowicz, A. Gössel, N. Mildner, and M. Dohlus, Beam tests of HOM absorber at FLASH, in *Proceedings of the International Particle Accelerator Conference, Kyoto, Japan, 2010* (ICR, Kyoto, 2010), pp. 4092–4094, https://accelconf.web.cern.ch/IPAC10/papers/thpec022.pdf.

[30] J. Baker-Jarvis, E. J. Vanzura, and W. A. Kissick, Improved technique for determining complex permittivity with the transmission/reflection method, IEEE Trans. Microwave Theory Tech. **38**, 1096 (1990).

[31] A. M. Nicolson and G. F. Ross, Measurement of the intrinsic properties of materials by time-domain techniques, IEEE Trans. Microwave Theory Tech. **19**, 377 (1970).

[32] W. B. Weir, Automatic measurement of complex dielectric constant and permeability at microwave frequencies, Proc. IEEE **62**, 33 (1974).

[33] T. Ota, M. Takasaki, S. Nakamura, A. Miyamoto, K. Sato, T. Konomi, K. Umemori, H. Sakai, and E. Kako,

Development of HOM absorbers for CW superconducting cavities in energy recovery linac, in *Proceedings of 18th International Conference on RF Superconductivity (SRF2017), Lanzhou, China* (JACoW, Geneva, Switzerland, 2018), pp. 191–193, 10.18429/JACoW-SRF2017-MOPB062.

[34] C. Kittel. *Introduction to Solid State Physics* (John Wiley & Sons, New York, 2004), 8th ed., ISBN 978-0471415268.

[35] T. Ota, M. Takasaki, S. Nakamura, A. Miyamoto, K. Sato, T. Konomi, K. Umemori, H. Sakai, and E. Kako, Development of HOM absorbers for CW superconducting cavities in energy recovery linac, in *Proceedings of 19th International Conference on RF Superconductivity, SRF2019, Dresden, Germany* (JACoW, Geneva, Switzerland, 2019), pp. 1060–1062, 10.18429/JACoW-SRF2019-THP072.